

Cite this: *J. Mater. Chem. A*, 2020, **8**, 1368

Evidence for interfacial geometric interactions at metal–support interfaces and their influence on the electroactivity and stability of Pt nanoparticles†

Xiao Zhao,^{‡*a} Takao Gunji,^{‡a} Takuma Kaneko,^{‡a} Shinobu Takao,^a Tomohiro Sakata,^a Kotaro Higashi,^a Yusuke Yoshida,^a Junjie Ge,^b Changpeng Liu,^b Wei Xing,^{‡*b} Jianbing Zhu,^c Meiling Xiao,^c Tomoya Uruga,^e Franklin (Feng) Tao,^d and Zhongwei Chen^{‡*c}

Supported metals are widely used as industrial catalysts wherein the supports affect catalytic performances remarkably through either electronic and/or geometric interactions with the metals, and/or providing interfacial synergistic sites. Herein, we observed evidence for interfacial geometric interactions (IGIs) at Pt–C interfaces through a combination of atomic-scale structural analysis, *in situ* X-ray absorption fine structure, and electrochemical measurements for Pt/C model systems. The IGI has a long-range attribute and affects Pt surface atoms not only at interfacial perimeters but also adjacent to interfaces. The affected Pt surface atoms are proposed to contribute enhanced activity and stability for the oxygen reduction reaction through retarding the formation of strongly adsorbed oxygenated intermediates. Our work provides some necessary information for a better understanding of support effects and catalytically active surface sites.

Received 12th November 2019
Accepted 15th December 2019

DOI: 10.1039/c9ta12456j

rsc.li/materials-a

Introduction

Supported metal atoms, clusters, and nanoparticles (NPs) are crucial materials in industrial catalysis.^{1–11} For electrocatalysis, metals, particularly Pt, supported on a spectrum of carbons are widely used for the oxygen reduction reaction (ORR), a key reaction in fuel cells and metal–air batteries.^{1–3,12–20} Both experiments and theoretical calculations reveal that the ORR overpotential on Pt originates from unfavorable –O and –OH binding energies that are about 0.2 eV and 0.1 eV stronger than the optimal values, respectively.^{21–27} To weaken Pt–O/OH binding energies, the general routes are the modulation of chemical compositions, shapes, and core–shell structures of Pt-based NPs and thus the production of geometric and/or

electronic/ligand effects.^{14,22} Supports are reported to be capable of affecting the selectivity and activity of supported metals through geometric and/or electronic interactions with metals,^{28,29} and/or interfacial synergistic effects.^{8,28,30,31} Assuming that the understanding and the control of support effects were addressed well, the supports may provide an opportunity for further improving Pt-based electrocatalysts.

Supports not only stabilize the metal particles but also change their electronic structure and can tune their catalytic activity.^{4,6,9,28,29,32–39} The first-principles study of metal adatom adsorption on graphene showed that adatoms from groups I–III exhibit characteristics of ionic bonding and large interfacial charge transfer (ICT) and work-function shifts. Transition metal atoms with d valence electrons, noble metals, and group IV elements display covalent bonding characteristics with strong hybridization of adatom and graphene electronic states.⁴⁰ For example, the hybridization between the π orbitals of the polyaromatic hydrocarbon surface and the d orbitals of the Pt adatoms enhances the back-donation of electrons to the $2\pi^*$ orbitals of the CO molecule.²⁹ Furthermore, the electron transfer may depend on the adsorption configuration of metals. Mahmoodinia *et al.* showed, through the DFT, that in a complex of Pt_n-polyaromatic hydrocarbon, the atomic charge is positive on the Pt atoms and the dimers with a parallel configuration, while a negative charge is found on the upper Pt atom of the Pt dimer with an upright configuration.^{29,33} On the other hand, in practical nanocatalysts, discrepancy exists in the literature with respect to the details of ICT even for the same system.^{6,35,36} For

^aInnovation Research Center for Fuel Cells, The University of Electro-Communications, Chofugaoka, Chofu, Tokyo 182-8585, Japan. E-mail: xiaozhao@uec.ac.jp

^bState Key Laboratory of Electroanalytical Chemistry, Changchun Institute of Applied Chemistry, Chinese Academy of Sciences, Changchun, Jilin 130022, China. E-mail: xingwei@ciac.ac.cn

^cDepartment of Chemical Engineering, University of Waterloo, Waterloo, Ontario, Canada. E-mail: zhwen@uwaterloo.ca

^dDepartment of Chemical and Petroleum Engineering, University of Kansas, Lawrence, KS 66045, USA

^eJapan Synchrotron Radiation Research Institute, SPring-8, Sayo, Hyogo 679-5198, Japan

† Electronic supplementary information (ESI) available: XRD, SEM, TEM/STEM/EDS, XAFS, and electrochemical data. See DOI: 10.1039/c9ta12456j

‡ These authors contributed equally: X. Z., T. G., and T. K.

instance, in the Pt–NbO_x or Pt–NbO_x/C system,^{6,35,36} ICT directions from Pt to O or from O to Pt,^{6,35,36} negligible ICT³⁷ and potential-dependent ICT⁶ were reported. Moreover, the charge screening effect from the metal NPs is argued to limit ICT at a sub-nm range.^{28,41}

On the other hand, the lattice strains can modulate metal d states and thus their binding energies to reactive intermediates, which consequently change the reactivity of the metals. The study of the effect of strain on the reactivity of metal surfaces was pioneered by Mavrikakis *et al.* by the DFT.⁴² The geometrical strain effect operates by shifting the local d-band of the involved metals up or down and thus tuning the reactivity of metals. For metals with more than half-filled d bands, the shortened interatomic distances (*e.g.* the geometrically compressive strain) increase the overlap of d-states and thus broaden the d-band; meanwhile to keep d-band filling constant, the d-band shifts downward.^{42–44} The metals with a downshifted d-band interact with the adsorbates in a weaker way and show a reduced reactivity. Compared with ICT, the lattice strains can influence metal atoms in a larger range,^{27,41,45} which is intriguing as the interfacial strain is theoretically demonstrated^{46,47} and/or experimentally observed^{48–52} due to the interfacial mismatch at metal–support interfaces. Gao *et al.* observed significant strain inside Au NPs near the stepped surfaces of rutile.⁵¹ The interfacial compressive strain was also seen in CoFe₂O₄ NPs supported on graphene oxide sheets.⁵⁰ However, the fine understanding of interfacial geometric interactions (IGIs, or, interfacial strains) and particularly their influence on the properties of metals remain difficult due to these reasons. (a) The metal–support interfaces are buried underneath metal NPs and thus hard to observe directly. (b) Both metal NPs and supports have structural heterogeneity in practical nanocatalysts. (c) The metal surfaces likely restructure in a reactive environment or during catalysis adopting geometric and electronic structures distinctly from their *ex situ* state. (d) The ICT and IGI are often interrelated in a catalyst and it is hard to distinguish their single contribution to catalysis. To this end, Resasco *et al.* recently highlighted catalyst characterization *via* a combination of site-specific atomic-level measurement, for example, *in situ* transmission electron microscopy (TEM) and sample-averaged techniques; for example, infrared spectroscopy is effective for the elucidation of the structure–property relationships of supported catalysts.⁵³ Due to heterogeneous surface sites on the metals, the additional complex issue is where the catalytically active sites are located. The surface atoms at interfacial perimeters have been frequently suggested as active sites for catalysis.^{8,46,54} Given the long-range attribute of IGI, the activated surface sites by IGI may be beyond interfacial perimeters.

In this work, we observed evidence for IGI by side-by-side comparing Pt/C model systems whose interfacial properties were controlled by the types of carbon support and the shapes and sizes of Pt NPs using a combination of atomic-scale structural analysis, *in situ* X-ray absorption fine structure (XAFS) and electrochemical measurements. The IGI benefits both the activity and stability of Pt NPs for the ORR, representing a desired structural effect for practical electrocatalysts. The Pt

surface atoms not only at interfacial perimeters but also adjacent to interfaces are suggested with enhanced ORR activity by the IGI effect.

Results and discussion

Atomic-scale evidence for the IGI

We hypothesized IGI having a “long-range” attribute and impacting surface atoms more than a few atomic layers far from stressed metal–support interfaces, as seen in core–shell structured NPs²⁷ and heterogeneous thin film systems.⁴⁵ Thus, it is possible to directly observe the influence of IGI, for example, changed interplanar spacings on metal NPs that have a thickness of only several atomic layers. To this end, ultrafine Pt NPs were controllably prepared and supported on two distinct carbon materials—carbon microcoils (CMCs, see Fig. S1, ESI†) and Ketjen Black (KB)—to produce different Pt–C interfacial properties. The controllable synthesis of size- and shape-uniform Pt NPs was conducted using a pH-tuned ethylene glycol reduction method (see Experimental details). The use of Pt/C is to avoid the alloying influences that can induce geometric and/or electronic effects. However, several structural factors still affect lattice strains of Pt NPs, for example, their sizes⁵⁵ and shapes.⁵⁶ Meanwhile, carbon surfaces are structurally complex resulting from their intrinsic structural defects, surface doping, chemically functional groups, surface curvature and so on, which is, unfortunately, hard to control at a statistical level. With careful considerations of structural heterogeneities from both Pt NPs and carbon surfaces, we thus analyze lattice strains at the single-particle level in order to reduce structural variables as much as possible. We imaged individual Pt NPs and carbon surfaces using aberration-corrected transmission electron microscopy (ATEM). Meanwhile, *in situ* XAFS and electrochemical measurements provide statistical-level structure–property information.

Fig. 1 shows ultrafine Pt NPs, uniformly distributed on carbon surfaces (Fig. 1a and b), which have an average size of about 2.1 nm (the insets in Fig. 1a and b) and adopt the shape of a cuboctahedron (Fig. 1c and d). As the free surfaces without constraint from the supports contract inward and appear coordination-dependent,⁵⁷ here to separate the origins of contraction from free surfaces and the influence of the support, we strictly compared the two particles that have the same size, shape/facet distribution, and composition. As such, the coordination number-dependent surface contraction will be the same for the two Pt NPs and their difference in lattice strains could be safely ascribed to the different interfacial properties. The two Pt NPs—KB-particle-1 from 2.1 nm Pt/KB and CMC-particle-1 from 2.1 Pt/CMC (Fig. 1c and d, respectively)—were selected because of their identical sizes and shapes. The averaged $d\{111\}$ spacing for CMC-particle-1 (Fig. 1f) is 2.21 Å, which appears compressive relative to the value of 2.29 Å for KB-particle-1 (Fig. 1e). In the $\{002\}$ orientation, a similar phenomenon but contraction to a different extent was observed (Fig. S2†). The anisotropic contraction at different orientations may originate from an anisotropic combination at Pt–CMC interfaces. As discussed above, the observed differences in

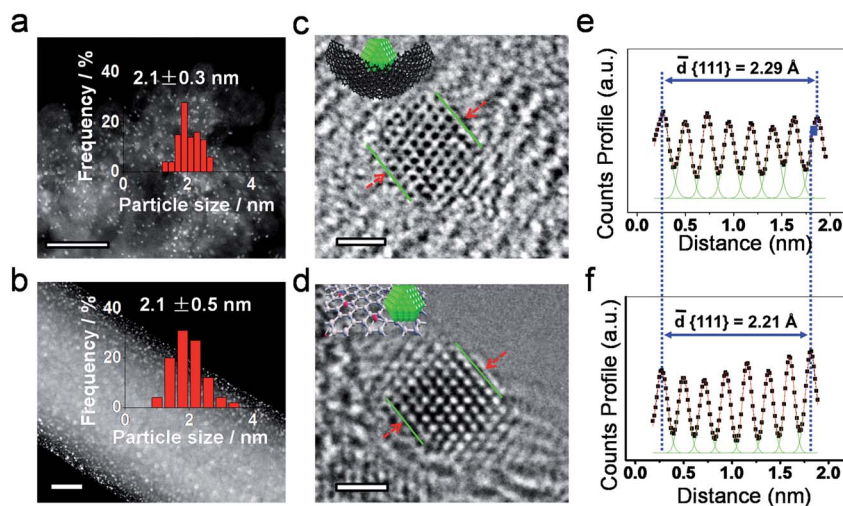


Fig. 1 Atomic-scale evidence for the IGI. (a and b) High-angle annular dark-field scanning transmission electron microscopy (HAADF-STEM) images for 2.1 nm Pt/KB (a) and 2.1 nm Pt/CMC (b). (c and d) Atomically resolved ATEM images for KB-particle-1 (c) and CMC-particle-1 (d). (e and f) Single-particle-based analysis of $d\{111\}$ interplanar spacing for KB-particle-1 (e) and CMC-particle-1 (f). Scale bars in (a and b) and (c and d) are 50 and 1 nm, respectively. The insets in (a and b) and (c and d) are particle size distribution histograms and possible geometric configurations of Pt NPs on carbon, respectively.

interplanar spacings between the two Pt NPs stem from distinct Pt–C interfacial properties and indicate the “long-range” attribute of IGI.²⁷

The supplementary evidence arises from observing two Pt NPs that are both from 2.1 nm Pt/CMC and have similar sizes but different interfacial areas, that is, CMC-particle-2 at the edge of CMC (Fig. 2a–c, g and h) and CMC-particle-3 completely supported by CMC (Fig. 2d–f). Interestingly, CMC-particle-3 with larger contact areas with CMC displays smaller interplanar spacings ($d\{111\} = 2.17 \text{ \AA}$), as compared with CMC-particle-2 ($d\{111\} = 2.26 \text{ \AA}$). The fine examination of CMC-particle-2 is shown in Fig. 2a and S3.† A much smaller $d\{111\}$ on the supported Pt region (2.18 \AA) than on the unsupported domain (2.37 \AA) was observed in CMC-particle-2. This is direct evidence for the existence of IGI because (i) supported and unsupported regions are in the identical nanoparticle with a small-enough size, about 2.3 nm; (ii) if there are any unknown factors, besides the IGI, affecting $d\{111\}$ spacing, these factors should have equivalent effects on supported and unsupported regions; (iii) the only sharp difference is with and without Pt–CMC interfaces between them. Additionally, in CMC-particle-2, we observed the local dislocations that initiate at the nanoscale border and develop toward the unsupported Pt domains presumably due to the uneven distribution of IGI. The dislocation is a kind of line defects and could induce local surface strain in lattices relative to the normal atomic arrangement. In this regard, the dislocation should affect the reactivity of NPs and deserves further study. In commercial Pt/C (TEC10E50E-HT, TTK), the Pt particle at the edges of carbon displays a similar phenomenon observed in CMC-particle-2 (Fig. S4†), thereby suggesting an extension of IGI to other carbon-supported metal systems. Notably, only statistically limited information obtained from the atomic-scale structural analysis is an inherent characteristic of the high-resolution TEM technique. Here, to make individual NPs more

representative of overall NPs, the main efforts were made in terms of controllable synthesis of shape- and size-uniform Pt NPs. Additional analysis of other Pt NPs from 2.1 nm Pt/CMC is shown in Fig. S5.†

In situ spectroscopic evidence for the IGI

To explore the influence of IGI on the ORR performances of Pt NPs, we utilized *in situ* XAFS, a sample-averaging technique, to characterize Pt NPs under the reaction conditions.^{58–60} *In situ* Pt L_3 -edge X-ray absorption near edge structure (XANES) spectra were collected as a function of applied potentials *versus* reversible hydrogen electrode (RHE). The *in situ* XANES data reveal that the normalized white-line peak intensities (μ_{norm}) of Pt L_3 -edge for both 2.1 nm Pt/CMC (Fig. 3a) and 2.1 nm Pt/KB (Fig. S6†) increase with applied potentials due to the chemisorption of oxygenated species on Pt surfaces.^{58,61–64} However, the strong oxygen adsorption was suppressed on 2.1 nm Pt/CMC at 1.0 V (Fig. 3b) compared to 2.1 nm Pt/KB. Furthermore, we analyzed the potential-dependent $\Delta\mu$ -XANES for the Pt- L_3 edge, which can reveal changes in the surface chemisorption of oxygenated species when changing potentials and represent a surface-sensitive technique.^{21,44–47,65} Pt L_3 -edge $\Delta\mu$ -XANES was obtained relative to the μ_{norm} at 0.4 V, a potential at double layers relatively free of surface adsorbates. As shown in Fig. 3c, the $\Delta\mu$ -XANES differs between the two catalysts. Specifically, when raising potentials from 0.4 to 0.8 V, the $\Delta\mu$ amplitudes are similar for the two catalysts; however, when elevating potentials from 0.8 to 1.0 V, a remarkably smaller $\Delta\mu$ amplitude was observed on 2.1 nm Pt/CMC than on 2.1 nm Pt/KB, suggesting inhibited adsorption of strongly bonded oxygenated species on 2.1 nm Pt/CMC. As it has been well documented that the compressive strains on Pt can shift the d-band center down and weaken the binding strength to

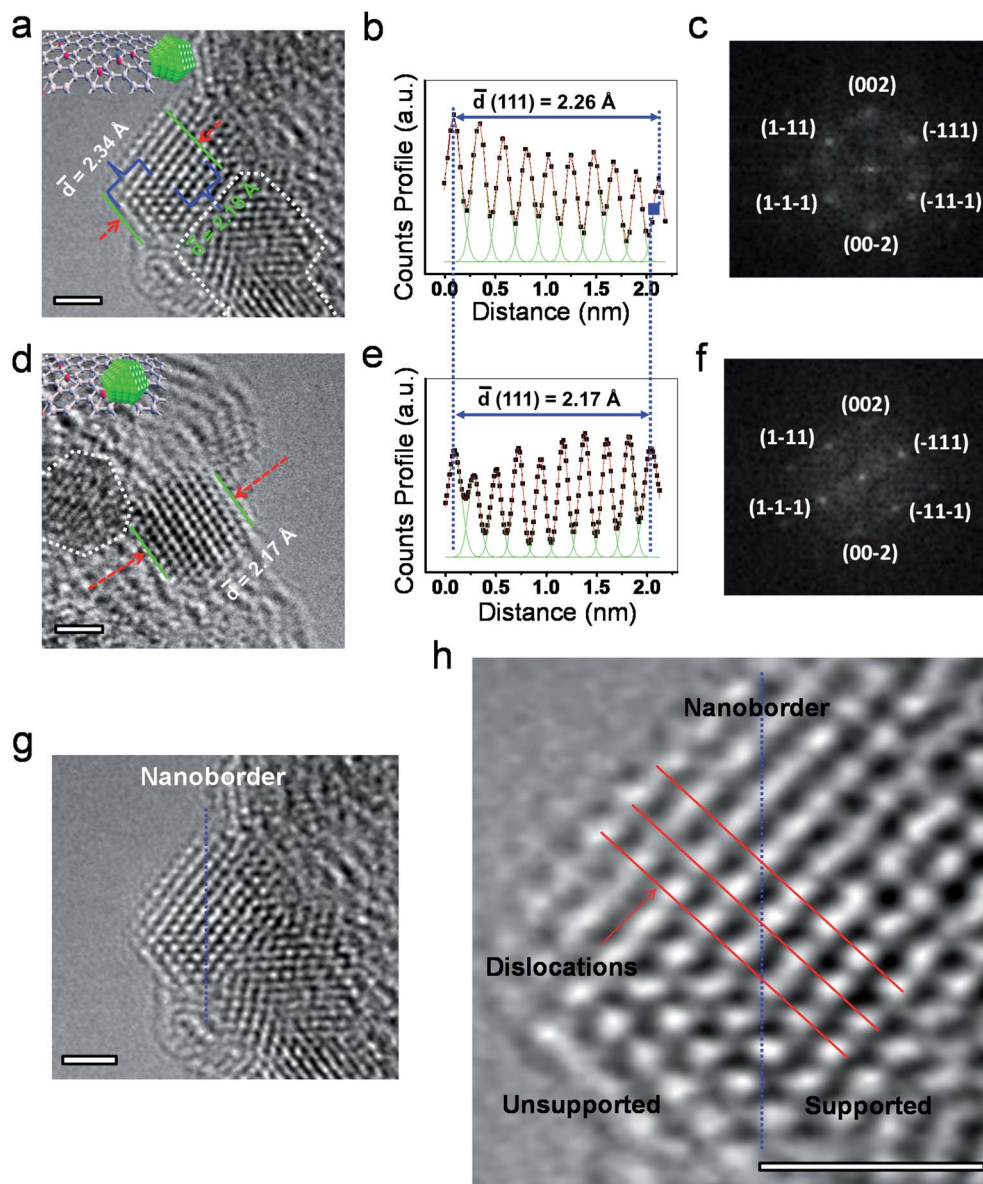


Fig. 2 Atomic-scale evidence for the IGI. (a, d, g and h) Atomically resolved ATEM images. (b and e) Analysis of $d\{111\}$ interplanar spacing. (c and f) Fast Fourier transform electron diffraction patterns. The Pt NPs in (a–c, g and h) and (d–f) are CMC-particle-2 and CMC-particle-3, respectively. The insets in (a and d) illustrate the discrepancy in interfacial areas between Pt NPs and CMC. Scale bars in (a, d, g and h) are 1 nm.

oxygenated species,^{25,27,42} the *in situ* XANES difference between the two catalysts is, thus, consistent with the observed compressive strains in 2.1 nm Pt/CMC as shown in the analysis of atomic-scale lattice strains. Extended X-ray absorption fine structure (EXAFS) spectra provide the local environment around the target atoms. The Fourier transformed EXAFS (FT-EXAFS) at 0.4 V in Fig. 3d shows that both 2.1 nm Pt/KB and 2.1 nm Pt/CMC did not present any scattering peaks that could be assigned to Pt–C or Pt–O shells except Pt–Pt peaks, suggesting that the possible ICT is too weak or too few (if any) to be visible in EXAFS.

The absence of strong ICT in 2.1 nm Pt/KB and 2.1 nm Pt/CMC helps the exploration of the IGI effect as the strong geometric and electronic interactions are often interrelated and

coexist in other systems.^{4,6,9,35–39} On the other hand, the fitted structures at 0.4 V (other results are in Table S1, ESI, Fig. S7 and S8†) reveal a shortened Pt–Pt bond distance of 2.741 ± 0.004 Å in 2.1 nm Pt/CMC compared to 2.749 ± 0.012 Å in 2.1 nm Pt/KB, in line with the atomic-scale analysis of lattice strains. The relatively small difference in Pt–Pt bond length between the two catalysts may be due to that the EXAFS is a sample-averaging technique and detects all atoms in a catalyst. Moreover, the extent of lattice strains or particle deformation depends strongly on the strength of metal–support interactions. Thus, an additional factor for only a small decrease in Pt–Pt bond length may be the moderate metal–C interactions in 2.1 nm Pt/CMC compared to other strong metal–metal oxide interactions. For instance, a clearly decreased Pt–Pt bond distance and a strong ICT have been detected by

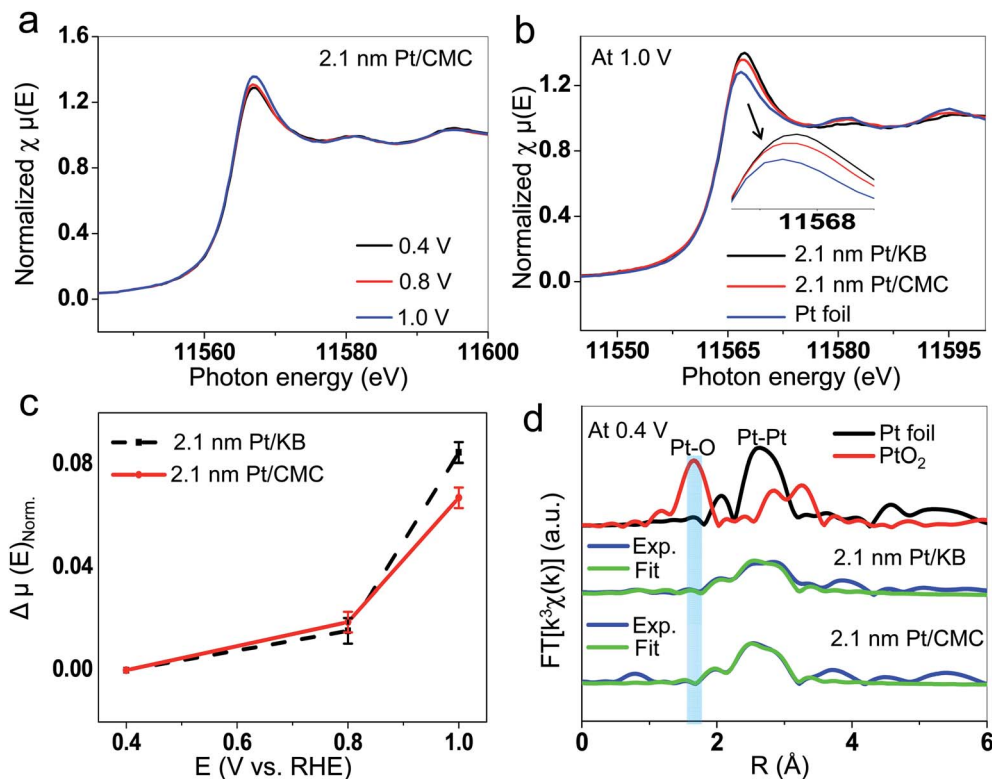


Fig. 3 *In situ* spectroscopic evidence for the IGI. (a and b) *In situ* Pt L_{3} -edge XANES spectra of 2.1 nm Pt/CMC and 2.1 nm Pt/KB. (c) *In situ* XANES analysis on Pt L_{3} -edge $\Delta\mu$. ($\Delta\mu = \mu(E)_{\text{norm}} - \mu_{\text{norm}}(0.4 \text{ V})$). (d) *In situ* k^3 -weighted Pt L_{3} -edge FT-EXAFS spectra at 0.4 V. The light blue rectangular region highlights that no Pt–C or Pt–O peaks can be assigned to 2.1 nm Pt/CMC and 2.1 nm Pt/KB.

EXAFS in the Pt/NbO_x/C system.⁶ However, the weak or negligible ICT as compared to the decent lattice strains in 2.1 nm Pt/CMC provides an opportunity to study the influence of IGI on the electrocatalytic performances of Pt NPs.

Influence of IGI on the electrocatalytic performances of Pt NPs

Enhanced ORR activity by the IGI. The ORR was used as a model reaction to scrutinize the influence of IGI on the electroactivity of Pt NPs. In Fig. 4a, the ORR polarization curves for 2.1 nm Pt/CMC show an anodic shift demonstrating its improved activity as compared with 2.1 nm Pt/KB. The calculated specific activity (SA, normalized by the electrochemical surface areas of Pt) and mass activity (MA, normalized by the mass of Pt) are about 2.1- and 2.0-times higher on 2.1 nm Pt/CMC than on 2.1 nm Pt/KB, respectively. A similar trend in ORR activity was observed for 2.1 nm Pt/CMC and commercial 2.0 nm Pt/C (TEC10E20E, Fig. S9†). From the combination of lattice strain analysis, *in situ* XAFS data, and previous studies,^{21–27} the improved SA on 2.1 nm Pt/CMC is ascribed mainly to IGI-induced compressive strains that shift the d-state of Pt surface atoms down and thus weaken their binding energies to ORR intermediates.

Size-dependent IGI effect. We explored a size-dependent IGI effect as the sizes of metal NPs affect overall interfacial areas and the fraction of surface atoms activated by IGI. As such, 5.0 nm Pt/CMC ($4.7 \pm 1.1 \text{ nm}$, Fig. S10†) and 5.0 nm Pt/C

(TEC10E50E-HT) were scrutinized. The 5.0 nm Pt/CMC still exhibited an enhanced SA relative to 5.0 nm Pt/C for the ORR (Fig. S11†), whereas its enhancement factor is about 1.5, which is smaller than the value of 2.1 for the 2.1 nm Pt/CMC. This size-dependent enhancement factor can be rationalized as that small-sized metal NPs have improved interfacial areas and an increased fraction of surface atoms that could be activated by the IGI. Notably, the metal clusters can present an unusual nonequilibrium nature during reactions including large structural disorder, librational motion of the center of mass, and fluctuating bonding.^{34,66,67} In this case, the dynamic flexible behaviour of metal clusters in order to respond to the reaction conditions may have a much larger effect than the long-range IGI discussed here.³⁴ To describe the dynamic physical picture for flexible nanoclusters tethered to the support surface needs a close combination of theoretical simulations and *operando* characterization techniques.

Improved ORR durability by the IGI. Robust stability with high activity is indispensable for practical electrocatalysts. We examined the influence of IGI on stability by an accelerated durability test (ADT) as shown in Fig. 4c. After 30 000 loading cycles between 0.6 and 1.0 V RHE, 2.1 nm Pt/CMC lost only 21.3% MA and appears much more stable than 2.1 nm Pt/KB (54.2% MA loss, Fig. 4d and S8†). Moreover, the STEM images and elemental distributions of 2.1 nm Pt/CMC between the initial state (Fig. 4e) and that after ADT (Fig. 4f) only show a small difference. These results demonstrate the improved

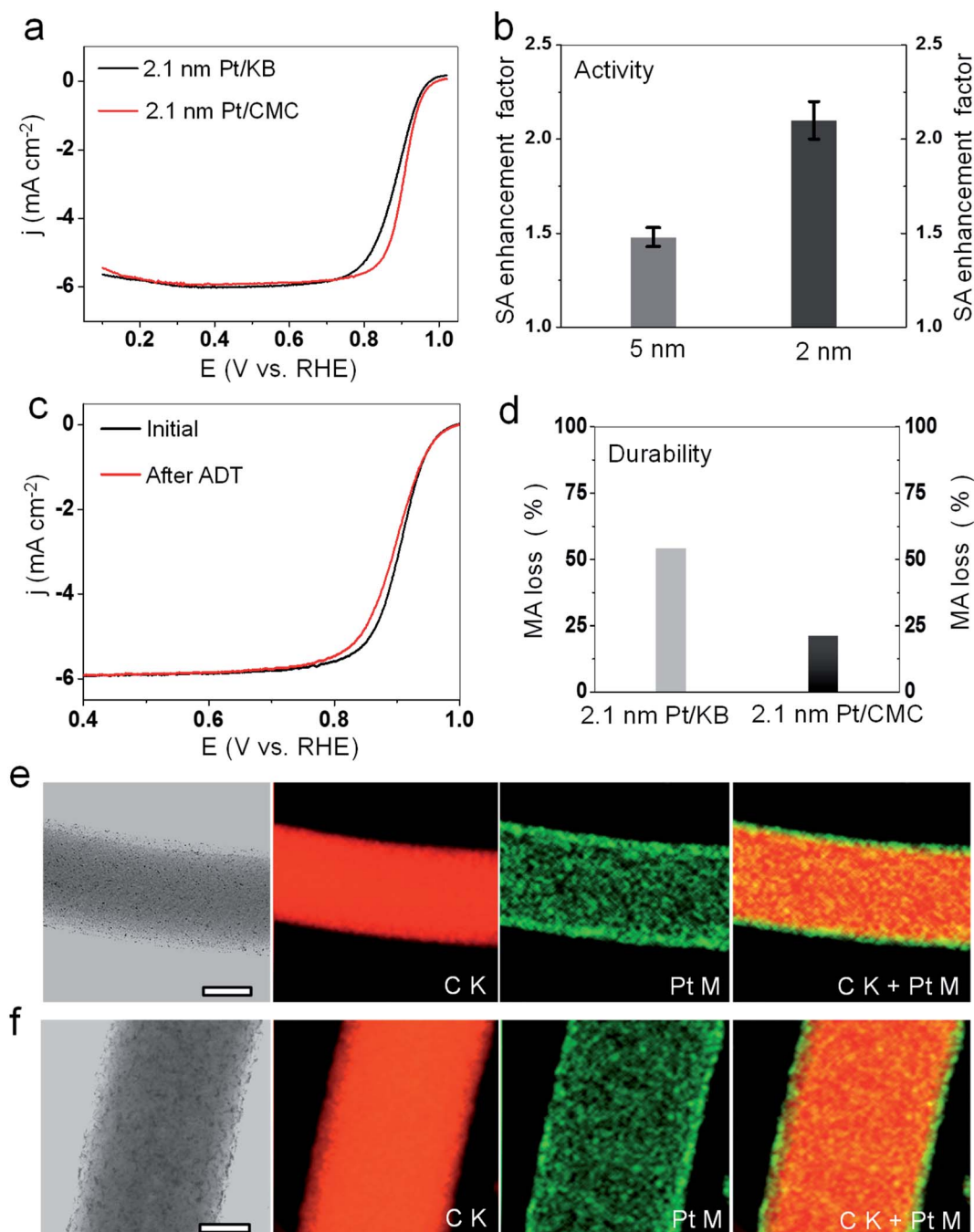


Fig. 4 Influences of the IGI on the activity and durability of Pt NPs for the ORR. (a) The ORR performances of catalysts evaluated *via* the anodic polarization in an O_2 -saturated 0.1 M $HClO_4$ electrolyte at 1600 rpm with IR correction. (b) Size-dependent enhancement factors induced by the IGI on the basis of comparisons of the specific activity (SA) for 4.7 nm Pt/CMC vs. 5.0 nm Pt/C (TEC10E50E-HT) and 2.1 nm Pt/CMC vs. 2.1 nm Pt/KB. (c) The durability of 2.1 nm Pt/CMC after 30 000 potential cycles. (d) Comparisons of the durability between 2.1 nm Pt/KB and 2.1 nm Pt/CMC according to their mass activity (MA) loss after the ADT. (e and f) STEM-EDS images for 2.1 nm Pt/CMC before (e) and after (f) ADT. Scale bars in (e) and (f) are 200 and 100 nm, respectively.

stability for 2.1 nm Pt/CMC probably due to the cooperative effect between Pt NPs and Pt–CMC interfaces: (i) Pt–C interfaces are buried underneath and thus protected by Pt NPs; (ii) in turn, the IGI weakens Pt–O/OH binding and inhibits the electrochemical oxidation and dissolution of Pt NPs. This cooperation makes IGI more robust compared to other non-precious metals

that induce lattice strain through an alloying effect but easily dissolve in a harsh ORR environment.

Interfacial strain field

Attributes of the IGI. Here, to discuss the influence of IGI on the electroactivity and stability of Pt NPs for the ORR, we

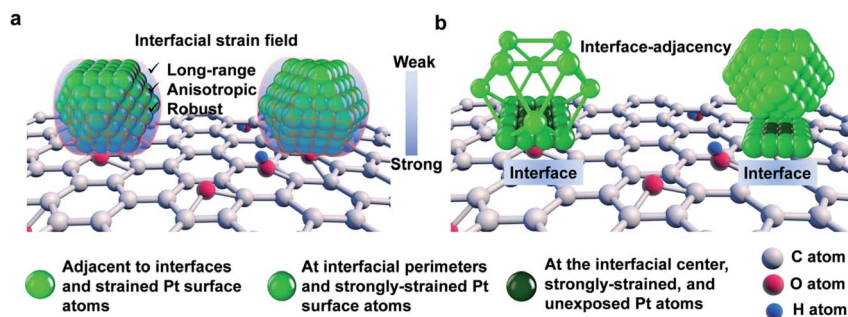


Fig. 5 Interfacial strain field model for the IGI. (a) Long-range, anisotropic and robust attributes for the IGI. Due to the atomic scale interphase or lattice mismatch at Pt–C interfaces (here Pt–CMC), the geometric strain initiates at Pt–C interfaces, evolves toward vicinal surface atoms and impacts their surface structure and catalytic behavior over several atomic layers far from the Pt–C interfaces. (b) Classification of surface sites in terms of their strained states and geometry locations. For clarity, a large part of Pt atoms was omitted in the particle at the left of (b). The upper portion of the particle at the right of (b) was raised to highlight the interfacial/interface-on Pt atoms.

introduce a model of interfacial strain field (ISF) in Fig. 5a. The IGI induces an interfacial strain field for Pt atoms both at the interfaces and adjacent to interfaces. The term “field” highlights the attribute of “long-range” impacting structures and the reactivity of Pt surface atoms more than a few atomic layers away from the interfaces.^{27,41,43,45} And the “anisotropy” attribute may be due to that the ISF varies at different crystallographic orientations (see the atomic-scale structural analysis). The “robust” attribute indicates the cooperative effect between Pt NPs and Pt–C interfaces making ISF more durable than do base metals (see the discussion in the stability section).

Pt surface atoms affected by the IGI. Based on the strained states and geometric positions, Pt atoms in a cuboctahedron are classified into three types (see Fig. 5b). The Pt atoms at the center of the interfaces are strongly strained but unexposed to ORR reactants. Secondly, the Pt atoms along interfacial perimeters are strongly strained and simultaneously available for ORR reactants. Thirdly, the Pt atoms adjacent to the interfaces are strained by the long-range IGI and also accessible for ORR reactants. The enhanced ORR activity is, thus, contributed by the Pt surface atoms not only at interfacial perimeters but also adjacent to the interfaces.

Possible factors affecting IGI. Herein, our observations suggest that smaller metal NPs, for example, 2 *versus* 5 nm, have a larger enhancement factor presumably due to an increased fraction of surface atoms activated by the IGI as compared with the larger NPs. Moreover, STEM energy dispersive spectroscopy (STEM-EDS) mapping shows that platinum highly overlaps with oxygen (Fig. S12[†]) because the oxygenated groups on the carbon surface often act as anchoring sites for adsorption of the metal precursor and subsequent deposition of metal NPs. On the other hand, the metal NPs at stepped surfaces or edges of the support are reported to strain or deform significantly.^{49,51} Here, the oxygenated groups on carbon surfaces may also promote IGI through strengthening the interfacial affinity to Pt NPs to some extent. Theoretical calculations showed that the larger the concentration of oxygenated groups is and the closer they are to the Pt adatom, the stronger is the Pt binding energy to the carbon support.³² However, there are huge complexities arising from both metals and supports in practical catalysts, the

differences in lattice strains between NPs occur even in a catalyst (see the above HRTEM analysis). A comprehensive discussion is beyond the scope of the current work and can be found in a recent review.²⁸

Conclusions

In summary, we provided evidence for the presence of interfacial geometric interactions (IGI) at metal–support interfaces on the basis of a combination of atomic-scale analysis of lattice strains, *in situ* XAFS, and electrochemical measurements. The IGI shows long-range, anisotropic and robust attributes and impacts the surface reactivity of the metals over several atomic layers far from the stressed metal–support interfaces. The surface atoms not only at interfacial perimeters but also vicinal interfaces are affected by the IGI and make their contribution to ORR activity enhancement. The current experimental findings and insights are expected to hold good for other metal–support systems.

Experimental section

Chemicals

Carbon micro-coils (CMCs) were provided by CMC General Research Institute in Gifu, Japan. Ethylene glycol, chloroplatinic acid hexahydrate, nitric acid, sodium hydroxide, and perchloric acid (TraceSELECT®) were all purchased from Sigma-Aldrich (research-grade) and used without further purification. Ultra-pure water (18 MΩ cm) purified in a Millipore system was used in all experiments.

Chemical activation of CMC

CMC was chemically activated using 3 M nitric acid solution at 60 °C for 48 h in which the surface graphene layer was partially oxidized to produce oxygenated species.

Preparation of 2.1 nm Pt/CMC, 2.1 nm Pt/KB and 4.7 nm Pt/CMC

Syntheses of 2.1 nm Pt/CMC, 2.1 nm Pt/KB and 4.7 nm Pt/CMC were based on an ethylene glycol reduction method as follows.

Taking 2.1 nm Pt/CMC as an example, 100 mg of CMC, 20 mL of ethylene glycol and 0.136 mL of 0.310 M chloroplatinic acid solution were added to a 150 mL pressure vessel. After 15 min stirring and 30 min ultra-sonication mixing, the pH of the mixing solution was adjusted to 10.0 using 0.1 M KOH solution. Then, the vessel was heated at 160 °C in an oil bath for 1 h. The obtained samples were filtered and rinsed using a mixture of ethanol and acetone ($v/v = 1/1$), followed by drying at 60 °C under vacuum. 2.1 nm Pt/KB was synthesized by a similar procedure except that 0.410 mL of 0.310 M chloroplatinic acid solution was added. 4.7 nm Pt/CMC was synthesized by a similar procedure without adjusting the pH. Commercial Pt/C with an average size of around 2.0 nm (TEC10E20E, 19.0 wt% Tanaka Kikinzoku Kogyo (TKK)) and Pt/C with an average size of 4–5 nm (TEC10E50E-HT, 50.9 wt% TKK) were also used for comparison.

Electrochemical measurements

All glassware for electrochemical measurements was treated with aqua regia and then with boiled water and washed with Millipore water thoroughly. A 0.1 M HClO₄ solution was prepared using perchloric acid (TraceSELECT®, Sigma-Aldrich) and 18.2 MΩ cm Millipore water. The electrocatalyst ink formulation was 1 mg electrocatalyst/0.5 mL Millipore water/0.4 mL isopropanol/0.005 mL 5 wt% Nafion®. The testing temperature was room temperature. Pt foil and RHE were used as the counter and reference electrodes, respectively. Electrocatalyst thin-film working electrodes were prepared by a spin coating method on a 5 mm rotating disk electrode (RDE). The Pt loading on the RDE was about 12.2 μg_{Pt} cm⁻². The working electrodes were treated by an electrochemical activation process over repeated potential cycles (typically 50 cycles) from 0.02 to 1.2 V at a scan rate of 100 mV s⁻¹ in N₂-saturated 0.1 M HClO₄ until a stable response was obtained. Cyclic voltammetry was performed at a scan rate of 50 mV s⁻¹ in N₂-saturated 0.1 M HClO₄. Electrocatalytic performances for the oxygen reduction reaction (ORR) were estimated by linear sweep voltammetry (LSV) from 0.0 to 1.05 V at a scan rate of 20 mV s⁻¹ in O₂-saturated 0.1 M HClO₄ at 1600 rpm. The measurements were repeated three times and the maximum current among them at 0.9 V was used for calculation of mass activity (MS) and surface-specific activity (SA). The solution resistance R_{sol} was measured by the i-interrupter method and used for IR-compensation. Accelerated durability test (ADT) for loading cycles: ADTs were conducted *via* rectangular-wave 0.6–1.0 V potential cycles of 3 s at each of 0.6 and 1.0 V up to 30 000 cycles in O₂-saturated 0.1 M HClO₄.

TEM and STEM-EDS

TEM and STEM samples were prepared by dispersing electrocatalysts in ethanol by sonication, putting the dispersed electrocatalysts on carbon film deposited on Cu grids, and drying. We measured the interplanar spacing using a state-of-the-art microscope JEM-ARM200F that allows observation of lattices with a spatial resolution of 0.7 Å (TEM mode). All imaging and analysis of interplanar spacing employed the same JEM-

ARM200F apparatus and followed the same method for the two catalysts (2.1 nm Pt/CMC and 2.1 nm Pt/KB). Expectedly, there is the same statistical error produced by imaging and analysis of interplanar spacing of Pt NPs for the two catalysts. Part of TEM and STEM-EDS images were measured on a JEM-2100F equipped with an energy dispersive spectrometer (EDS) at 200 kV.

In situ X-ray absorption fine structure (XAFS)

All electrodes used for *in situ* XAFS measurement were electrochemically pretreated by a procedure that is same with electrocatalytic measurements except for particular statements. Electrocatalysts covered on rotating disk electrodes (RDEs) were used as the working electrode for *in situ* XAFS in N₂-saturated 0.1 M HClO₄ in a home-made electrochemical cell at 1600 rpm. The measurements of *in situ* XAFS spectra at the Pt L₃-edge were performed in fluorescence mode by using a Si(111) double-crystal monochromator and an ion chamber (I_0 : Ar 5%/N₂ 95%) for incident X-rays and a 21 Ge-element detector for fluorescent X-rays at the BL36XU station in SPring-8 similar to the previous reports.^{58,60} X-ray absorption near-edge structure (XANES) spectra were normalized using Athena software. The XAFS spectra were treated with the data analysis program IFEFFIT (version 1.2.11c). Theoretical phase shifts and amplitude functions for Pt–Pt were calculated using FEFF 8.4. The extracted EXAFS oscillations were k^3 -weighted and Fourier transformed to R -space. The curve fittings of k^3 -weighted EXAFS data in R -space were carried out with an Artemis.

XRD

X-ray diffraction patterns were measured on a Rigaku RINT2000 with Cu K α irradiation at 40 kV and 40 mA in the 2θ range of 10–90° at a step scan speed of 0.02° s⁻¹.

XRF

X-ray fluorescence (XRF) analysis for bulk composition was conducted with a Rigaku ZSX Primus2.

Author contributions

X. Z., W. X., and Z. W. C. proposed and discussed the possible interfacial geometric interactions at metal-support interfaces. X. Z. synthesized the electrocatalysts. X. Z., W. X., and Z. W. C. co-wrote the manuscript. X. Z., J. B. Z., M. L. X., J. J. G. and C. P. L. conducted electrochemical experiments and discussed data. X. Z., T. K., Y. Y., T. S., K. H., and T. U. conducted *in situ* RDE-XAFS tests. X. Z. and T. G. conducted high-resolution TEM, STEM and EDX measurement. Y. Y. and X. Z. conducted SEM measurements. S. T. measured partial STEM images. F. T. provided constructive suggestions. All authors read and commented the manuscript.

Conflicts of interest

There are no conflicts to declare.

Acknowledgements

This work was supported by the New Energy and Industrial Technology Development Organization (NEDO) of Japan. This work was supported by the New Energy and Industrial Technology Development Organization (NEDO) of the Ministry of Economy, Trade, and Industry (METI), Japan. The financial support from the National Natural Science Foundation of China (21633008), the National Key R&D Program of China (Grant No. 2017YFB0102900) is appreciated. The authors appreciate the financial support from the Natural Sciences and Engineering Research Council of Canada (NSERC), the University of Waterloo, and the Waterloo Institute of Nanotechnology. The XAS measurements were performed with the approval of SPRING-8 subject number 2018A7806, 2018B7800, 2019A7800 and 2019B7800. A part of HR-TEM measurements was conducted under the support of the NIMS microstructural characterization platform as a program of the “Nanotechnology Platform” of the Ministry of Education, Culture, Sports, Science, and Technology (MEXT), Japan. We thank the help of Y. Iwasawa for this project and his suggestion for utilizing CMC as the support. We thank Dr S. Motojima, President of CMC Advanced R&D Lab. Co. Ltd for providing CMC samples. F. T. acknowledges financial support from Chemical Sciences, Geosciences and Biosciences Division, Office of Basic Energy Sciences, Office of Science, U.S. Department of Energy, under Grant No. DE-SC0014561 and the NSF Career Award NSF-CHE-14162121.

References

- Z. W. Seh, J. Kibsgaard, C. F. Dickens, I. Chorkendorff, J. K. Nørskov and T. F. Jaramillo, *Science*, 2017, **355**, eaad4998.
- M. K. Debe, *Nature*, 2012, **486**, 43–51.
- H. A. Gasteiger, S. S. Kocha, B. Sompalli and F. T. Wagner, *Appl. Catal., B*, 2005, **56**, 9–35.
- S. J. Tauster, S. C. Fung and R. L. Garten, *J. Am. Chem. Soc.*, 1978, **100**, 170–175.
- Y. Liu and W. E. Mustain, *J. Am. Chem. Soc.*, 2013, **135**, 530–533.
- Q. Jia, S. Ghoshal, J. Li, W. Liang, G. Meng, H. Che, S. Zhang, Z.-F. Ma and S. Mukerjee, *J. Am. Chem. Soc.*, 2017, **139**, 7893–7903.
- J. A. Horsley, *J. Am. Chem. Soc.*, 1979, **101**, 2870–2874.
- J. An, Y. Wang, J. Lu, J. Zhang, Z. Zhang, S. Xu, X. Liu, T. Zhang, M. Gocyla, M. Heggen, R. E. Dunin-Borkowski, P. Fornasiero and F. Wang, *J. Am. Chem. Soc.*, 2018, **140**, 4172–4181.
- S. J. Tauster, *Acc. Chem. Res.*, 1987, **20**, 389–394.
- J. C. Matsubu, S. Y. Zhang, L. DeRita, N. S. Marinkovic, J. G. G. Chen, G. W. Graham, X. Q. Pan and P. Christopher, *Nat. Chem.*, 2017, **9**, 120–127.
- X. Zhao, J. Zhu, L. Liang, J. Liao, C. Liu and W. Xing, *J. Mater. Chem.*, 2012, **22**, 19718–19725.
- Z. P. Cano, D. Banham, S. Ye, A. Hintennach, J. Lu, M. Fowler and Z. Chen, *Nat. Energy*, 2018, **3**, 279–289.
- A. Rabis, P. Rodriguez and T. J. Schmidt, *ACS Catal.*, 2012, **2**, 864–890.
- A. Chen and P. Holt-Hindle, *Chem. Rev.*, 2010, **110**, 3767–3804.
- M. Shao, Q. Chang, J.-P. Dodelet and R. Chenitz, *Chem. Rev.*, 2016, **116**, 3594–3657.
- I. E. L. Stephens, A. S. Bondarenko, U. Gronbjerg, J. Rossmeisl and I. Chorkendorff, *Energy Environ. Sci.*, 2012, **5**, 6744–6762.
- M. Li, Z. Zhao, T. Cheng, A. Fortunelli, C.-Y. Chen, R. Yu, Q. Zhang, L. Gu, B. V. Merinov, Z. Lin, E. Zhu, T. Yu, Q. Jia, J. Guo, L. Zhang, W. A. Goddard III, Y. Huang and X. Duan, *Science*, 2016, **354**, 1414–1419.
- X. Huang, Z. Zhao, L. Cao, Y. Chen, E. Zhu, Z. Lin, M. Li, A. Yan, A. Zettl, Y. M. Wang, X. Duan, T. Mueller and Y. Huang, *Science*, 2015, **348**, 1230–1234.
- C. Chen, Y. Kang, Z. Huo, Z. Zhu, W. Huang, H. L. Xin, J. D. Snyder, D. Li, J. A. Herron, M. Mavrikakis, M. Chi, K. L. More, Y. Li, N. M. Markovic, G. A. Somorjai, P. Yang and V. R. Stamenkovic, *Science*, 2014, **343**, 1339–1343.
- X. Tian, X. Zhao, Y.-Q. Su, L. Wang, H. Wang, D. Dang, B. Chi, H. Liu, E. J. M. Hensen, X. W. Lou and B. Y. Xia, *Science*, 2019, **366**, 850–856.
- J. K. Nørskov, J. Rossmeisl, A. Logadottir, L. Lindqvist, J. R. Kitchin, T. Bligaard and H. Jónsson, *J. Phys. Chem. B*, 2004, **108**, 17886–17892.
- A. Kulkarni, S. Siahrostami, A. Patel and J. K. Nørskov, *Chem. Rev.*, 2018, **118**, 2302–2312.
- V. R. Stamenkovic, B. Fowler, B. S. Mun, G. F. Wang, P. N. Ross, C. A. Lucas and N. M. Markovic, *Science*, 2007, **315**, 493–497.
- J. Greeley, I. E. L. Stephens, A. S. Bondarenko, T. P. Johansson, H. A. Hansen, T. F. Jaramillo, J. Rossmeisl, I. Chorkendorff and J. K. Nørskov, *Nat. Chem.*, 2009, **1**, 552–556.
- V. Stamenkovic, B. S. Mun, K. J. J. Mayrhofer, P. N. Ross, N. M. Markovic, J. Rossmeisl, J. Greeley and J. K. Nørskov, *Angew. Chem., Int. Ed.*, 2006, **45**, 2897–2901.
- V. Viswanathan, H. A. Hansen, J. Rossmeisl and J. K. Nørskov, *ACS Catal.*, 2012, **2**, 1654–1660.
- P. Strasser, S. Koh, T. Anniyev, J. Greeley, K. More, C. Yu, Z. Liu, S. Kaya, D. Nordlund, H. Ogasawara, M. F. Toney and A. Nilsson, *Nat. Chem.*, 2010, **2**, 454–460.
- I. C. Gerber and P. Serp, *Chem. Rev.*, 2019, DOI: 10.1021/acs.chemrev.9b00209.
- M. Mahmoodinia, P.-O. Åstrand and D. Chen, *J. Phys. Chem. C*, 2016, **120**, 12452–12462.
- M. Xu, S. Yao, D. Rao, Y. Niu, N. Liu, M. Peng, P. Zhai, Y. Man, L. Zheng, B. Wang, B. Zhang, D. Ma and M. Wei, *J. Am. Chem. Soc.*, 2018, **140**, 11241–11251.
- T. Lunkenbein, J. Schumann, M. Behrens, R. Schlögl and M. G. Willinger, *Angew. Chem., Int. Ed.*, 2015, **54**, 4544–4548.
- M. Mahmoodinia, P.-O. Åstrand and D. Chen, *J. Phys. Chem. C*, 2017, **121**, 20802–20812.
- M. Mahmoodinia, M. Ebadi, P.-O. Åstrand, D. Chen, H.-Y. Cheng and Y.-A. Zhu, *Phys. Chem. Chem. Phys.*, 2014, **16**, 18586–18595.

- 34 M. Mahmoodinia, T. T. Trinh, P.-O. Åstrand and K.-Q. Tran, *Phys. Chem. Chem. Phys.*, 2017, **19**, 28596–28603.
- 35 L. Zhang, L. Y. Wang, C. M. B. Holt, T. Navessin, K. Malek, M. H. Eikerling and D. Mitlin, *J. Phys. Chem. C*, 2010, **114**, 16463–16474.
- 36 L. Zhang, L. Y. Wang, C. M. B. Holt, B. Zahiri, Z. Li, K. Malek, T. Navessin, M. H. Eikerling and D. Mitlin, *Energy Environ. Sci.*, 2012, **5**, 6156–6172.
- 37 K. Sasaki, L. Zhang and R. R. Adzic, *Phys. Chem. Chem. Phys.*, 2008, **10**, 159–167.
- 38 L. Zhang, L. Wang, C. M. B. Holt, T. Navessin, K. Malek, M. H. Eikerling and D. Mitlin, *J. Phys. Chem. C*, 2010, **114**, 16463–16474.
- 39 T. Ioannides and X. E. Verykios, *J. Catal.*, 1996, **161**, 560–569.
- 40 K. T. Chan, J. B. Neaton and M. L. Cohen, *Phys. Rev. B: Condens. Matter Mater. Phys.*, 2008, **77**, 235430.
- 41 H. Wang, S. Xu, C. Tsai, Y. Li, C. Liu, J. Zhao, Y. Liu, H. Yuan, F. Abild-Pedersen, F. B. Prinz, J. K. Nørskov and Y. Cui, *Science*, 2016, **354**, 1031–1036.
- 42 M. Mavrikakis, B. Hammer and J. K. Nørskov, *Phys. Rev. Lett.*, 1998, **81**, 2819–2822.
- 43 M. Luo and S. Guo, *Nat. Rev. Mater.*, 2017, **2**, 17059.
- 44 S. Schnur and A. Groß, *Phys. Rev. B: Condens. Matter Mater. Phys.*, 2010, **81**, 033402.
- 45 R. C. Cammarata, *Prog. Surf. Sci.*, 1994, **46**, 1–38.
- 46 E. D. Hermes, G. R. Jenness and J. R. Schmidt, *Mol. Simul.*, 2015, **41**, 123–133.
- 47 B. Liu, J. Liu, T. Li, Z. Zhao, X. Q. Gong, Y. Chen, A. J. Duan, G. Y. Jiang and Y. C. Wei, *J. Phys. Chem. C*, 2015, **119**, 12923–12934.
- 48 E. Ochoa-Fernández, D. Chen, Z. Yu, B. Tøtdal, M. Rønning and A. Holmen, *Surf. Sci.*, 2004, **554**, L107–L112.
- 49 T. Daio, A. Staykov, L. M. Guo, J. F. Liu, M. Tanaka, S. M. Lyth and K. Sasaki, *Sci. Rep.*, 2015, **5**, 13126.
- 50 A. Mishra, *J. Mater. Sci.*, 2017, 7677–7687.
- 51 W. Gao, A. S. Choi and J.-M. Zuo, *Surf. Sci.*, 2014, **625**, 16–22.
- 52 J. A. Enterkin, K. R. Poepfelmeier and L. D. Marks, *Nano Lett.*, 2011, **11**, 993–997.
- 53 J. Resasco, S. Dai, G. Graham, X. Pan and P. Christopher, *J. Phys. Chem. C*, 2018, **122**, 25143–25157.
- 54 M. Konsolakis, *Appl. Catal., B*, 2016, **198**, 49–66.
- 55 M. Klimentov, S. Nepijko, H. Kuhlenbeck, M. Bäumer, R. Schlögl and H. J. Freund, *Surf. Sci.*, 1997, **391**, 27–36.
- 56 J. B. Wu, L. Qi, H. J. You, A. Gross, J. Li and H. Yang, *J. Am. Chem. Soc.*, 2012, **134**, 11880–11883.
- 57 W. J. Huang, R. Sun, J. Tao, L. D. Menard, R. G. Nuzzo and J. M. Zuo, *Nat. Mater.*, 2008, **7**, 308.
- 58 X. Zhao, S. Takao, K. Higashi, T. Kaneko, G. Samjeské, O. Sekizawa, T. Sakata, Y. Yoshida, T. Uruga and Y. Iwasawa, *ACS Catal.*, 2017, **7**, 4642–4654.
- 59 X. Zhao, T. Gunji, T. Kaneko, Y. Yoshida, S. Takao, K. Higashi, T. Uruga, W. He, J. Liu and Z. Zou, *J. Am. Chem. Soc.*, 2019, **141**, 8516–8526.
- 60 K. Nagasawa, S. Takao, S.-i. Nagamatsu, G. Samjeské, O. Sekizawa, T. Kaneko, K. Higashi, T. Yamamoto, T. Uruga and Y. Iwasawa, *J. Am. Chem. Soc.*, 2015, **137**, 12856–12864.
- 61 S. Mukerjee, S. Srinivasan, M. P. Soriaga and J. McBreen, *J. Electrochem. Soc.*, 1995, **142**, 1409–1422.
- 62 F. W. Lytle, P. S. P. Wei, R. B. Gregor, G. H. Via and J. H. Sinfelt, *J. Chem. Phys.*, 1979, **70**, 4849–4855.
- 63 Q. Jia, W. Liang, M. K. Bates, P. Mani, W. Lee and S. Mukerjee, *ACS Nano*, 2015, **9**, 387–400.
- 64 M. Teliska, W. E. O'Grady and D. E. Ramaker, *J. Phys. Chem. B*, 2005, **109**, 8076–8084.
- 65 X. Zhao, S. Takao, T. Kaneko and Y. Iwasawa, *Chem. Rec.*, 2019, **19**, 1337–1353.
- 66 F. Vila, J. J. Rehr, J. Kas, R. G. Nuzzo and A. I. Frenkel, *Phys. Rev. B: Condens. Matter Mater. Phys.*, 2008, **78**, 121404.
- 67 Y. He, J.-C. Liu, L. Luo, Y.-G. Wang, J. Zhu, Y. Du, J. Li, S. X. Mao and C. Wang, *Proc. Natl. Acad. Sci. U. S. A.*, 2018, **115**, 7700–7705.